

BME 695

November 1, 2011

Engineering Nanomedical Systems

Lecture 13

Designing nanodelivery systems for in-vivo use

James F. Leary, Ph.D.

SVM Endowed Professor of Nanomedicine
Professor of Basic Medical Sciences and
Biomedical Engineering

Member: Purdue Cancer Center; Oncological Sciences Center;
Bindley Biosciences Center; Birck Nanotechnology Center

Email: jfleary@purdue.edu

13.1 Bringing in-vivo considerations into NMS design

13.1.1 the in-vitro to ex-vivo to in-vivo paradigm

13.1.1.1 In-vitro - importance of choosing suitable cell lines

13.1.1.2 adding the complexity of in-vivo background while keeping the simplicity of in-vitro

13.1.1.3 all the complexity of ex-vivo plus the “active” components of a real animal

13.1 Bringing in-vivo considerations into NMS design (continued)

- 13.1.2 In-vivo systems are open, “active” systems with multiple layers of complexity
 - 13.1.2.1 In-vitro and ex-vivo are mostly “closed” systems, but not absolutely
 - 13.1.2.2 What is an “open” system?
 - 13.1.2.3 Attempts to isolate open systems

13.1 Bringing in-vivo considerations into NMS design (continued)

13.1.3 Layers of complexity of in-vivo systems

13.1.3.1 Human cells in nude mice – a mixture of in-vitro and in-vivo

13.1.3.2 “Model” small animal systems

13.1.3.3 better model larger animal systems

13.2 Circulation time and biodistribution

13.2.1 factors affecting circulation time

13.2.1.1 size/shape

13.2.1.2 "stealth layer" coating

13.2.1.3 zeta potential in-vivo in
varying environments

13.2.1.4 filtration and excretion

13.2.1.5 dose/targeting

13.2 Circulation time and biodistribution (continued)

13.2.2. where do the NMS go in-vivo?

13.2.2.1 checking the obvious organs (liver,
spleen, kidney, blood...)

13.2.2.2 finding NMS in tissues and organs

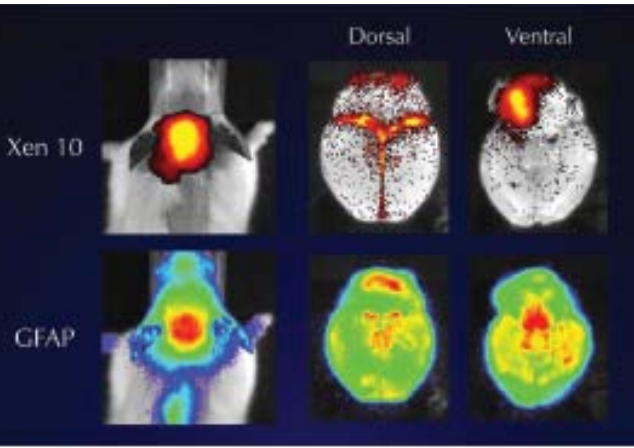
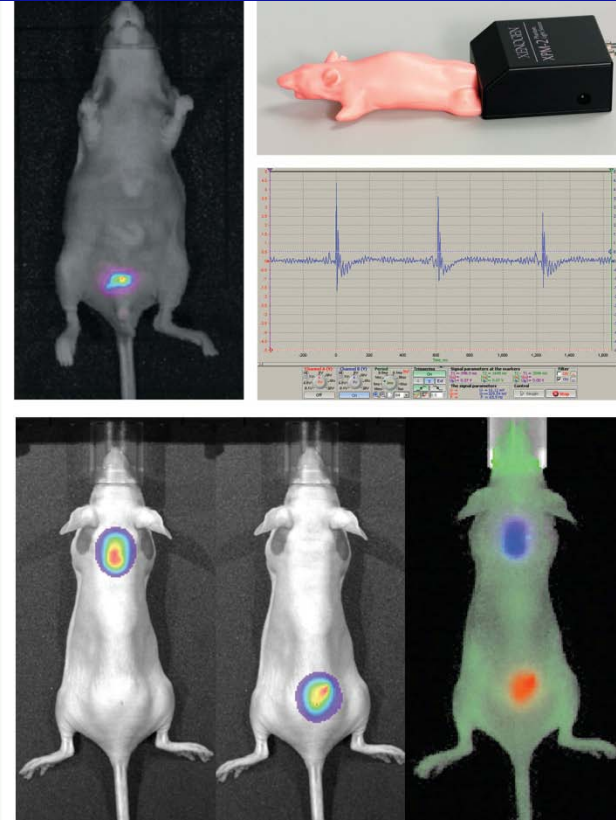
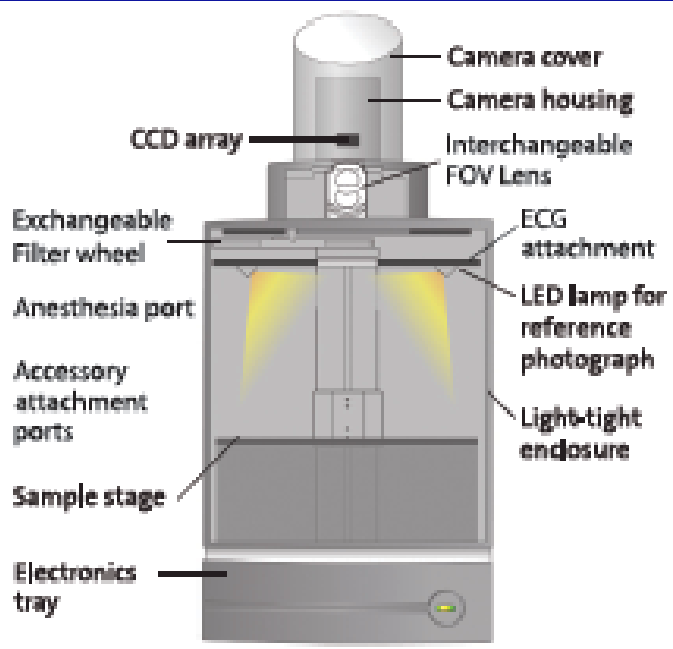
13.2.2.2.1 in-vivo

13.2.2.2.2 within dissected tissue sections

13.2.2.2.3 in blood (ex-vivo versus in-vivo
flow cytometry)

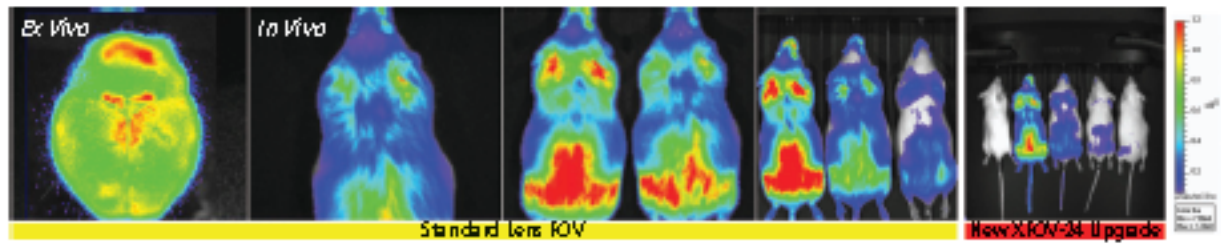
13.2.2.2.4. what is excreted?

Near Infrared Fluorescence (NIRF) Imaging



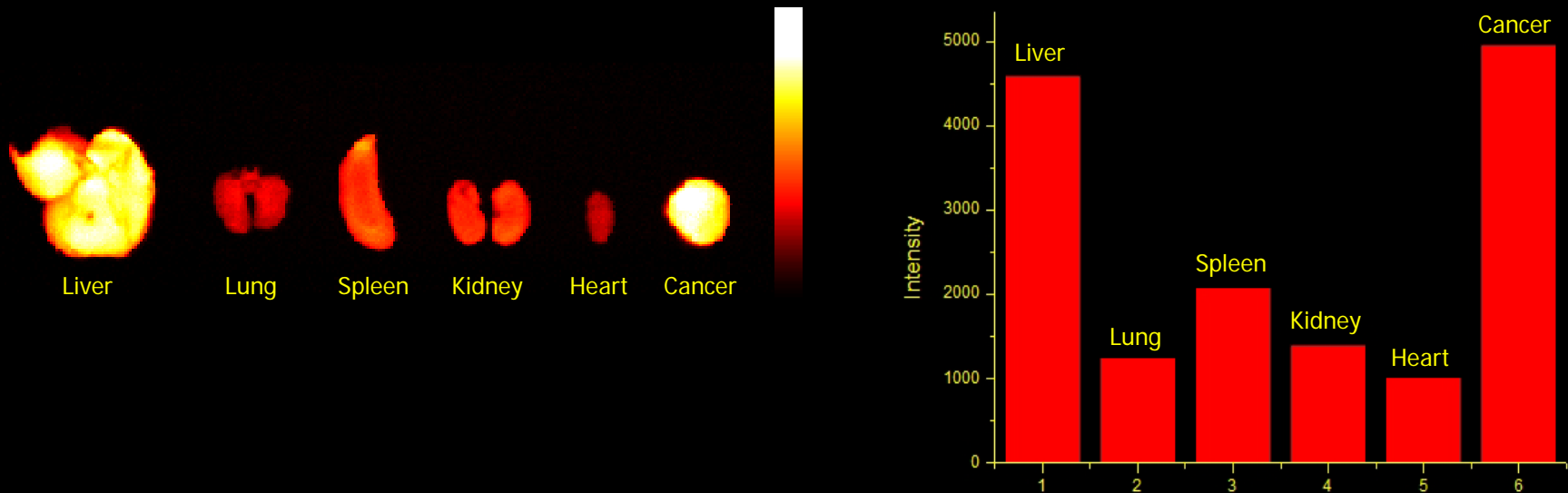
Dual Reporter Imaging - High Resolution Ex Vivo Applications

Field of View



The MIS Lumina II Imaging System provides 5 fields of view.

Ex vivo results of HGC-Cy5.5-SPIOs

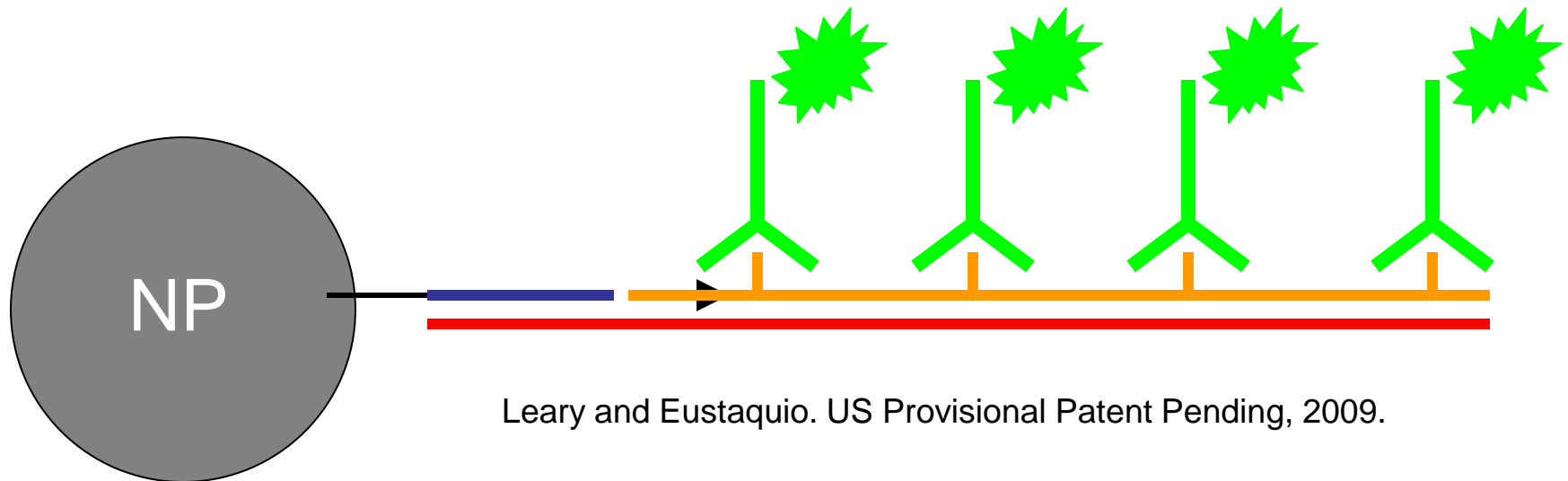


Ex vivo results means that most NPs were accumulated in cancer and liver. The accumulation in liver is a problem still remained. It might cause by large size or less flexibility of the NPs. However, when comparing current drugs available, it is still meaningful in terms of that the NPs were mostly accumulated in cancer.

Problem: How to find “suboptical-sized nanoparticles in a tissue?

Proposed solution: Use DNA barcoding

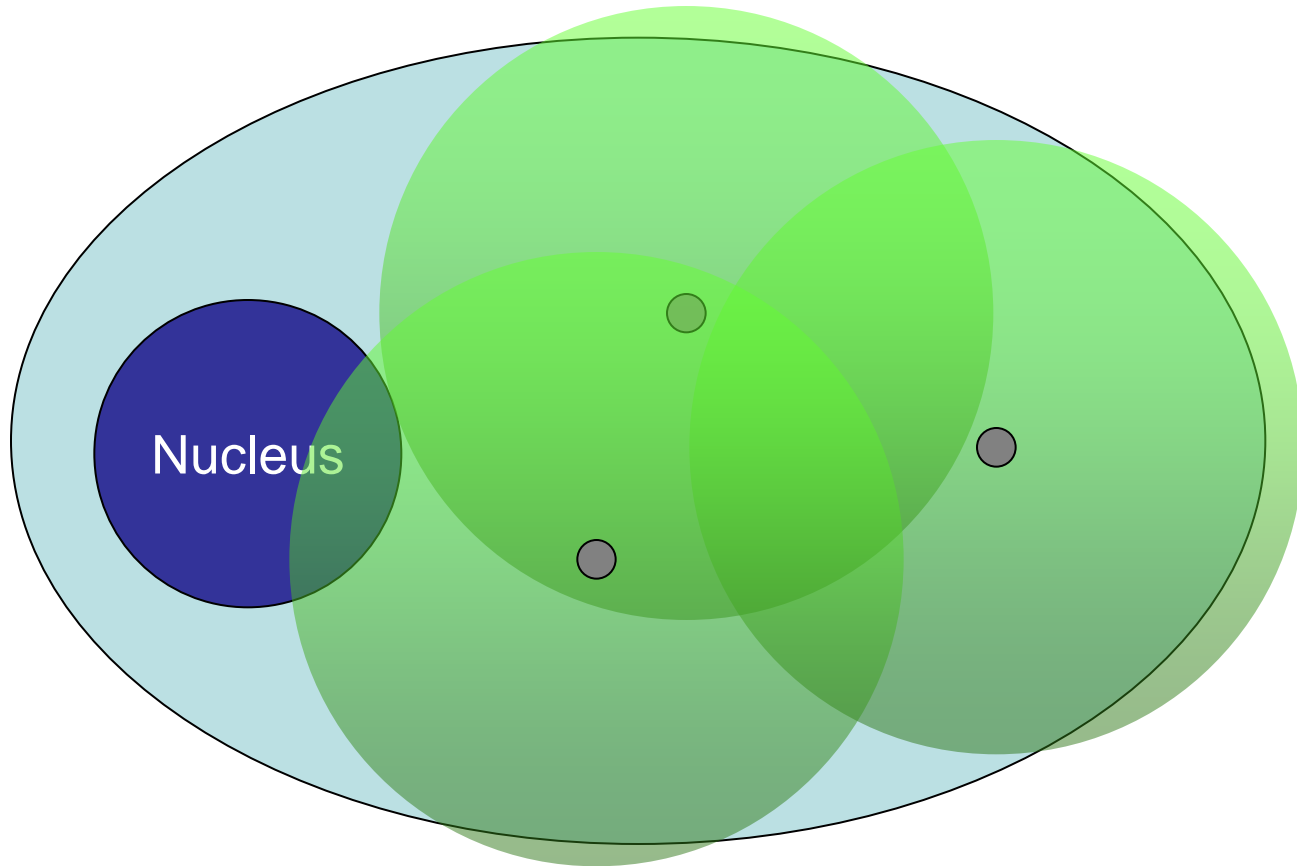
- Incorporate a DNA oligonucleotide “barcode” onto nanoparticles that can be detected inside fixed cells and tissue by *in situ* PCR*



Leary and Eustaquio. US Provisional Patent Pending, 2009.

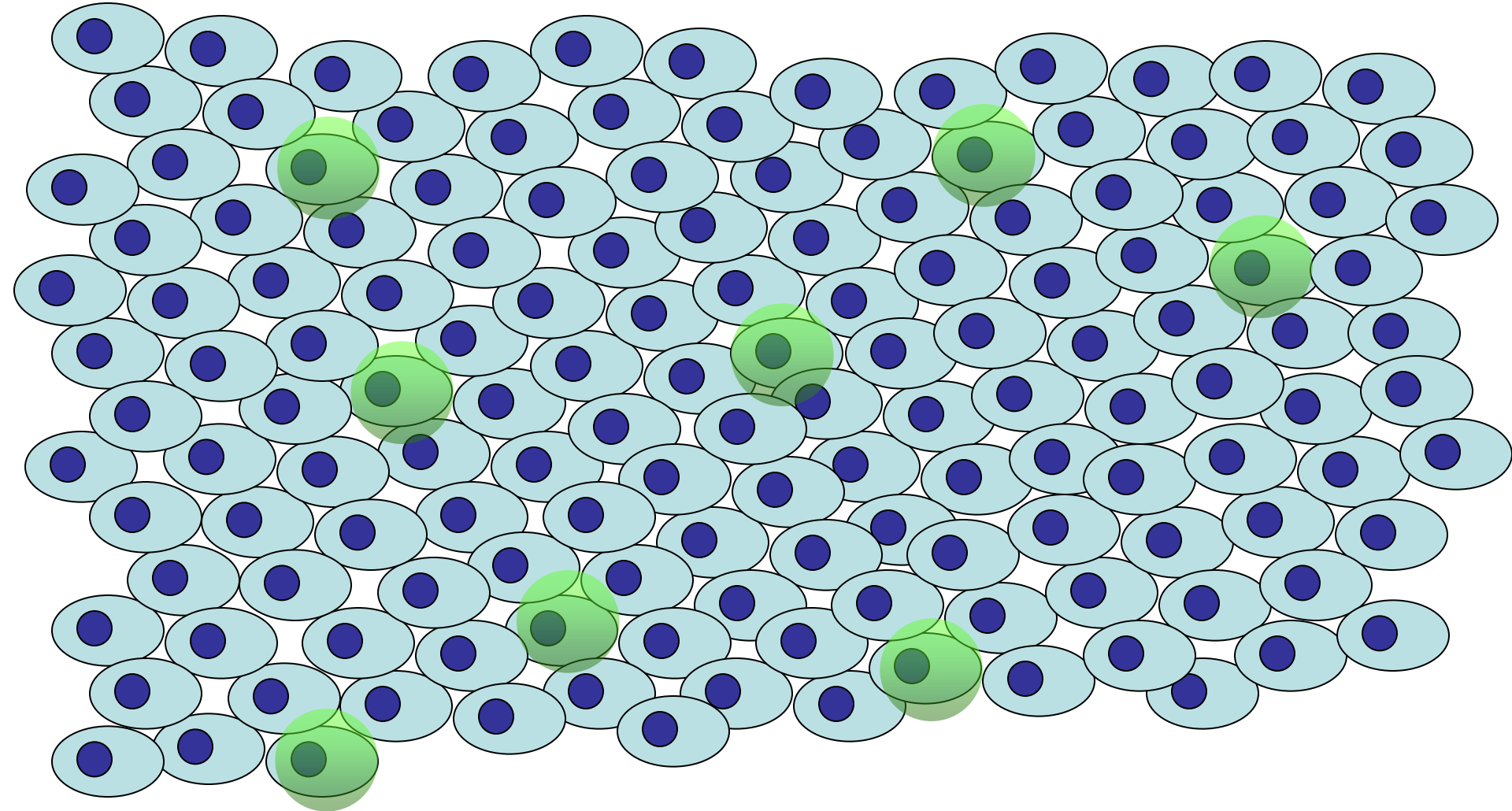
* Bagasra, 2007; Nuovo, 1997

Labeled PCR products (amplicons) form an optically sized diameter of detectable (by scanning image cytometry) signal around each nanoparticle



Theoretically we can see a single nanoparticle in a cell after in-situ PCR.

DNA barcode in-situ PCR-amplified nanoparticle signals enable rapid detection of small numbers of nanoparticles over large areas in tissues



So this tells us where to look, in more detail, over large areas of tissue.

In-vivo distributions of nanoparticles

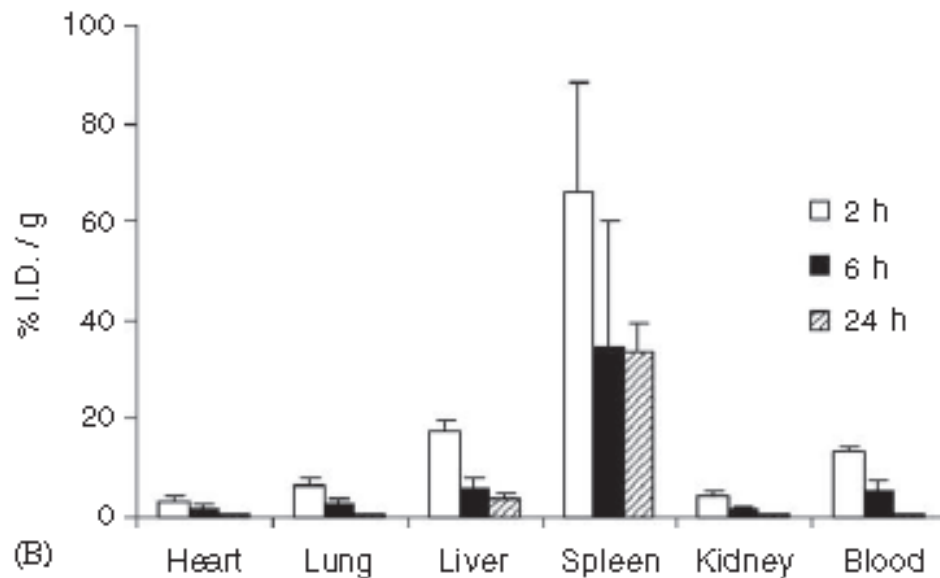
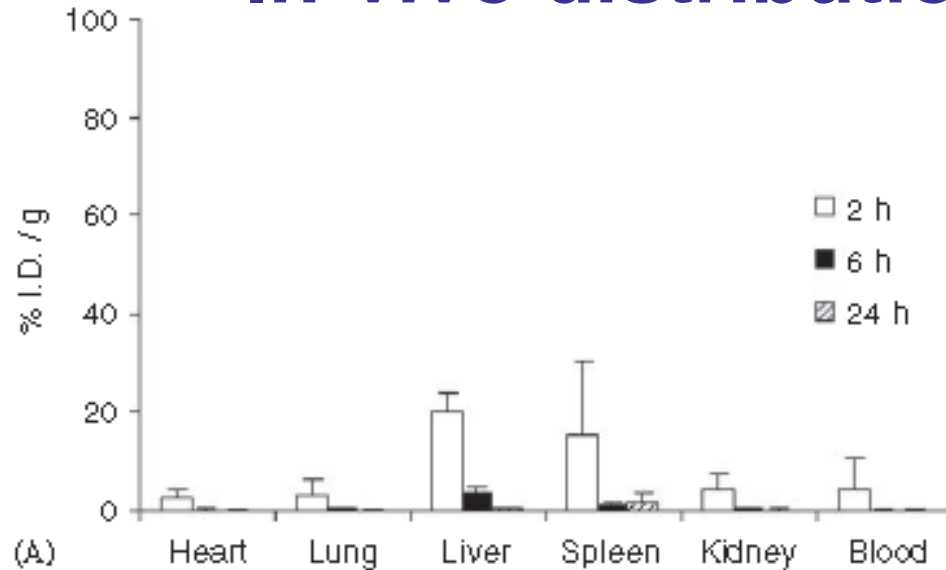


Fig. 7. Systemic biodistribution of (A) PLGA-b-PEG NP and (B) NP-Apt (mean \pm SD; n = 4).

Source: Cheng et al. 2007

In-vivo biodistribution of radiolabeled nanoparticles

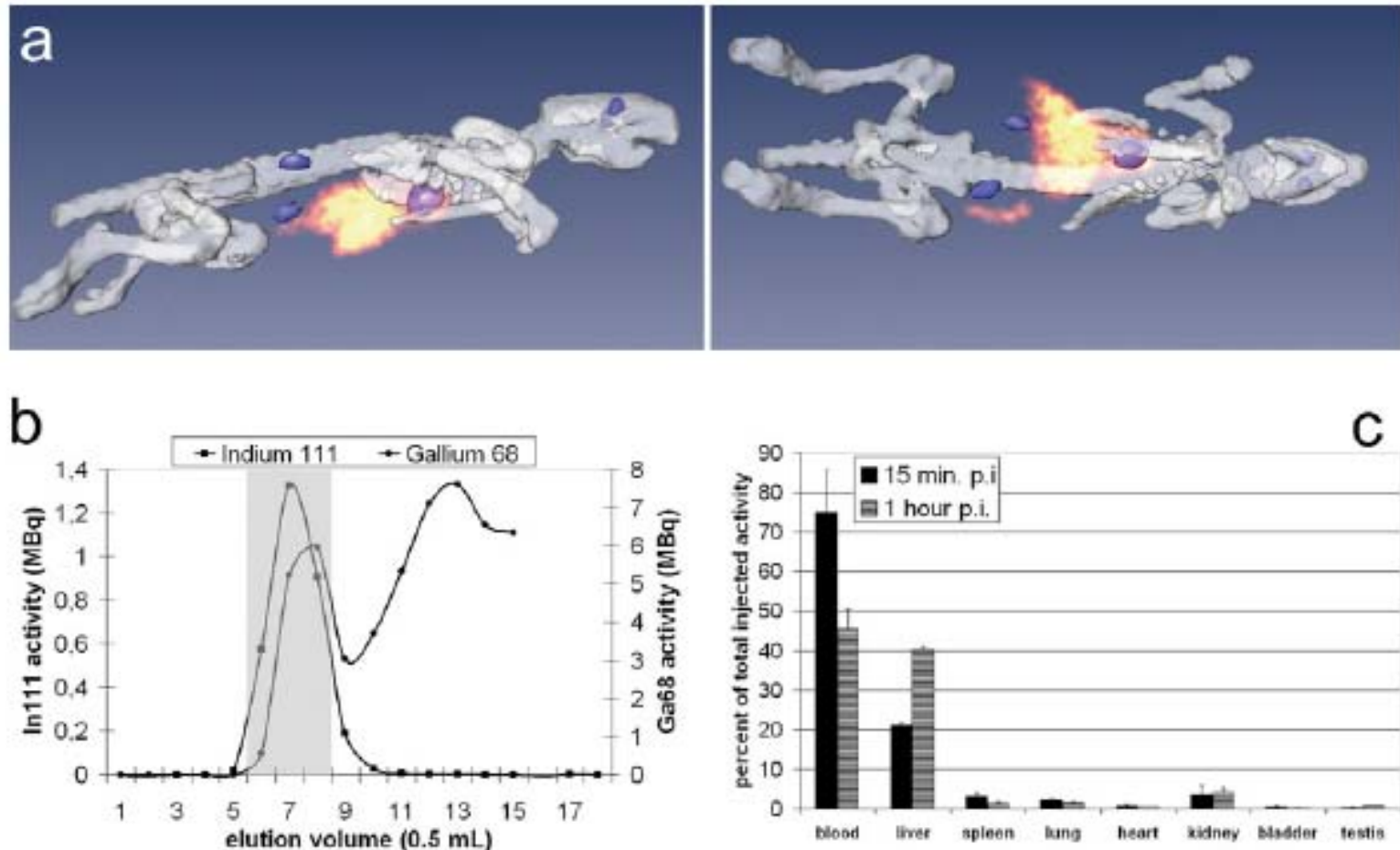


Figure 1. Radiolabelling of EPMA nanoparticles and in vivo biodistribution following intravenous injection. Wistar rats were injected intravenously with ^{68}Ga -labelled nanoparticles and scanned using an animal PET device after 13 min ((a); yellow and red signal). For a rough anatomical assignment rats were treated in independent experiments with ^{18}F -fluoride for skeleton and cartilage imaging (grey) and with ^{18}F -deoxyglucose revealing eyes, heart and kidney (blue). The resulting data sets were 3D reconstructed, superposed and aligned using Amira™. Two pictures from different angles are shown (a). See also the movie file provided in the supplement (available at stacks.iop.org/Nano/18/195102). (b) Elution profile of nanoparticle solutions after direct labelling with ^{68}Ga or ^{111}In . 95% of the loaded nanoparticles were collected in fractions 6–8 (shaded region). In (c) ^{111}In -labelled nanoparticles were applied and radioactivity was measured in extracted organs and blood samples at indicated time points.

Source: Cartier et al., 2007

Interaction of rhodamine B-labelled EPMA nanoparticles with blood components using flow cytometry

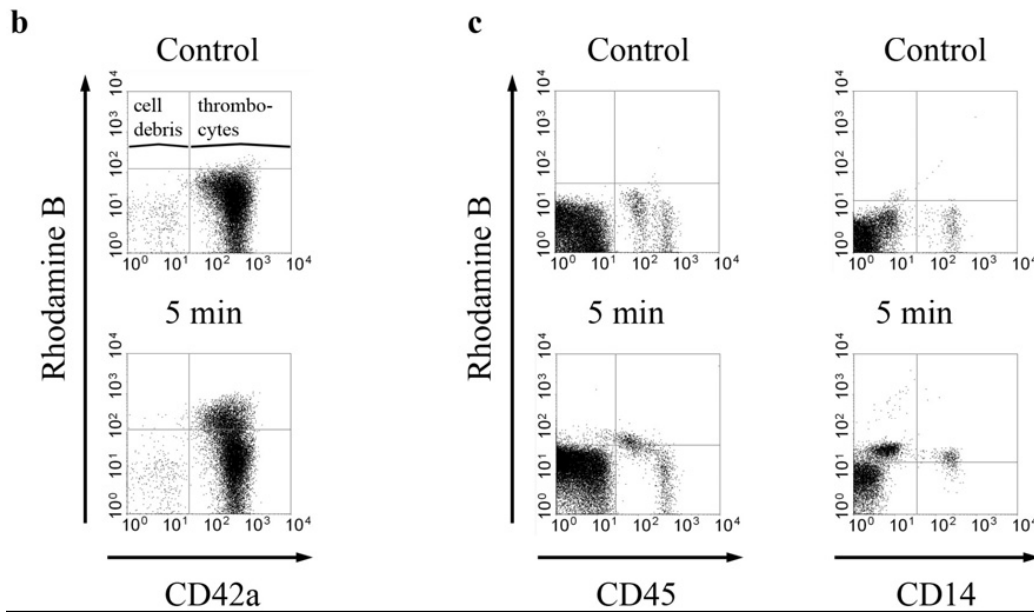
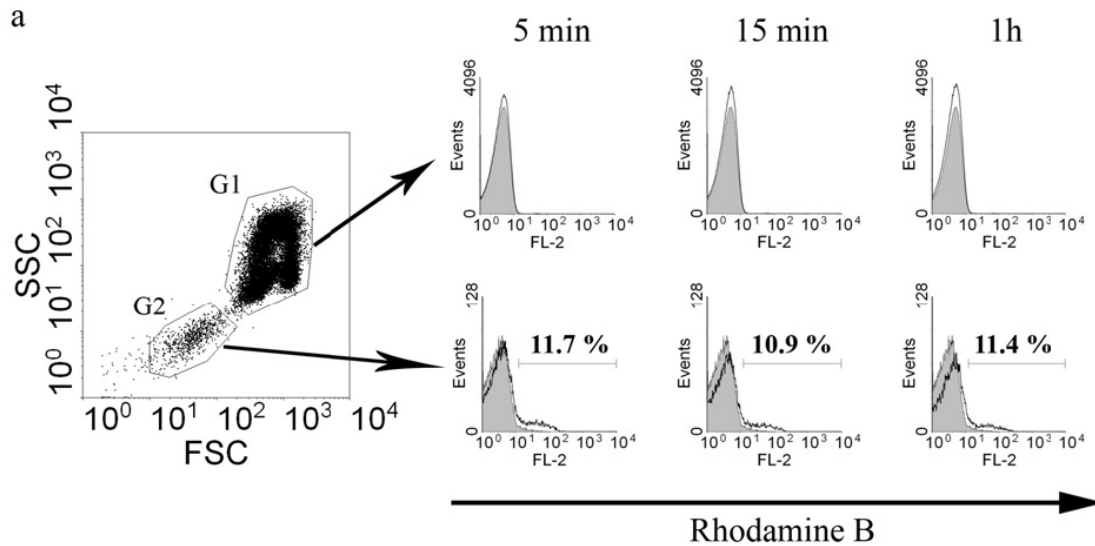


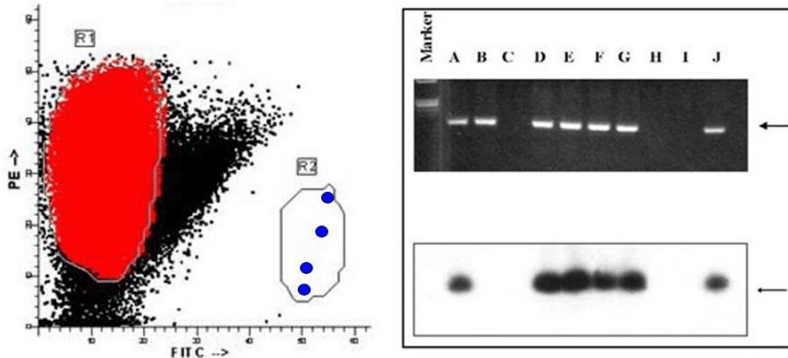
Figure 3. Interaction of rhodamine B-labelled EPMA nanoparticles with blood components using flow cytometry. Rhodamine B-labelled nanoparticles were incubated with whole blood corresponding to previous in vivo experiments. Representative data from three independent experiments are shown. Diluted whole blood was first analysed by the scattered plot to distinguish between erythrocytes (G1) and thrombocytes plus cell debris (G2). Association of rhodamine B-labelled nanoparticles to the gated cell components was then assessed at indicated time points. Controls correspond to $t = 0$ (shaded histogram) (a). Thrombocytes were further distinguished from cell debris in G2 by CD42a expression analysis using a monoclonal FITC-labelled antibody. The control corresponds to $t = 0$ (b). Similarly, interactions with leucocytes were analysed through CD45- or CD14 surface expression (c). In these experiments, erythrocytes were lysed prior to flow cytometry. Controls are untreated cells. **Source: Cartier, 2007.**

Use of Ultra-High Speed Flow Cytometry and Cell Sorting to Select Targeting Aptamers and to Evaluate Targeting to Rare Cells for Nanomedicine

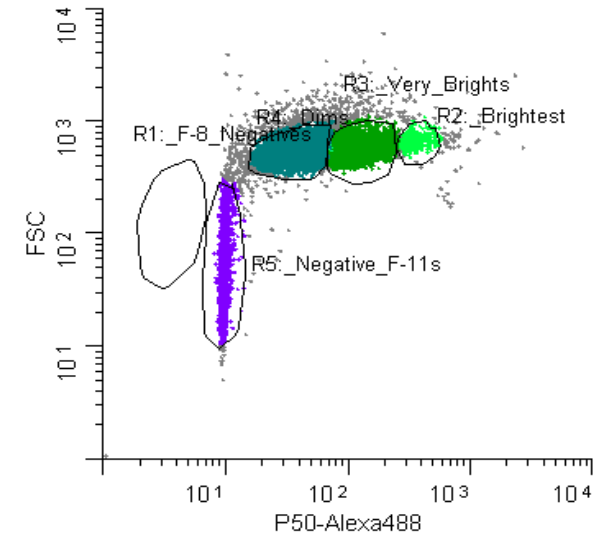
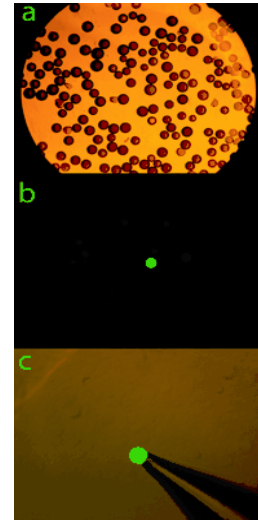


This high-speed flow cytometer/cell sorter is the world's fastest instrument and is used for separating rare cells or particles of interest.

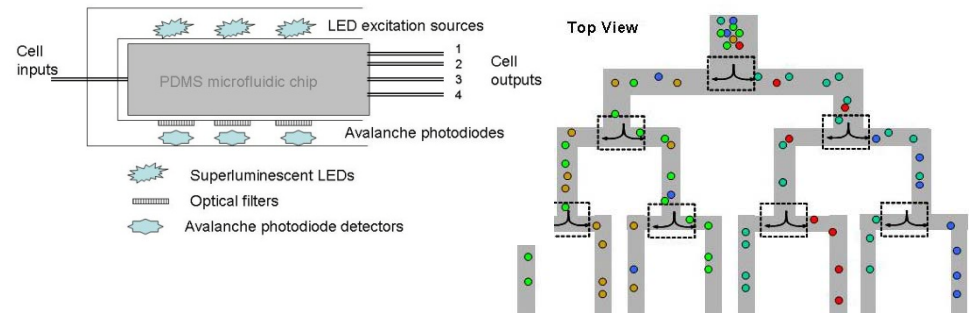
New technologies for the detection and isolation of very rare tumor cells in cancer patients



Early cancer detection and monitoring of patients in remission requires very high-speed detection, isolation and molecular characterization technologies for rare single tumor cells (●).



Sorting of thioaptamer combinatorial chemistry library beads with bound protein, is one way to isolate a specific drug. Up to 100 million drug candidates can be screened in a single day using high-throughput technologies.



A high-speed (>10,000 cells/sec), portable (PDA-sized), commercially manufacturable, multi-stage BioMEMS microfluidic cell sorter.

15.2 Circulation time and biodistribution (continued)

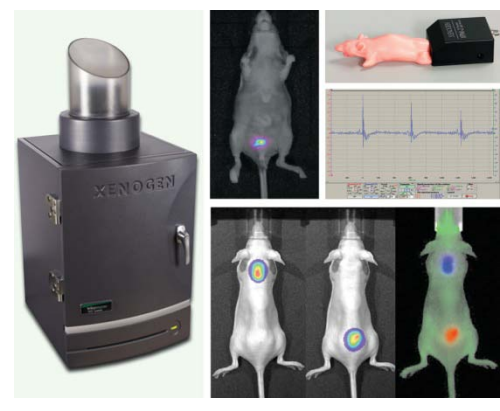
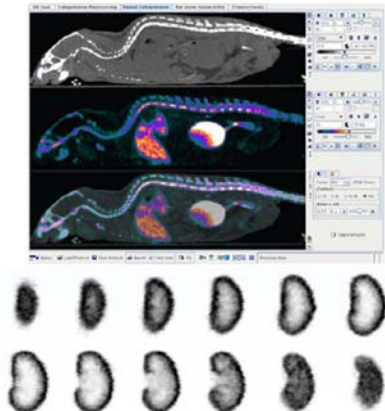
13.2.3 Circulation time and dose optimization

13.2.3.1 measure drug concentration
over time







13.2.3.2 is there an optimal drug dose?

13.4 In-vivo targeting and mistargeting

- 13.4.1 mode of administration (intravenous, oral, intra-tumor)
- 13.4.2 how can we assess targeting in-vivo? (MRI, fluorescence,...)
- 13.4.3 a rare-cell targeting problem
- 13.4.4 consequences of mistargeting
- 13.4.5 balancing dosing, therapeutic efficacy, and consequences of mistargeting



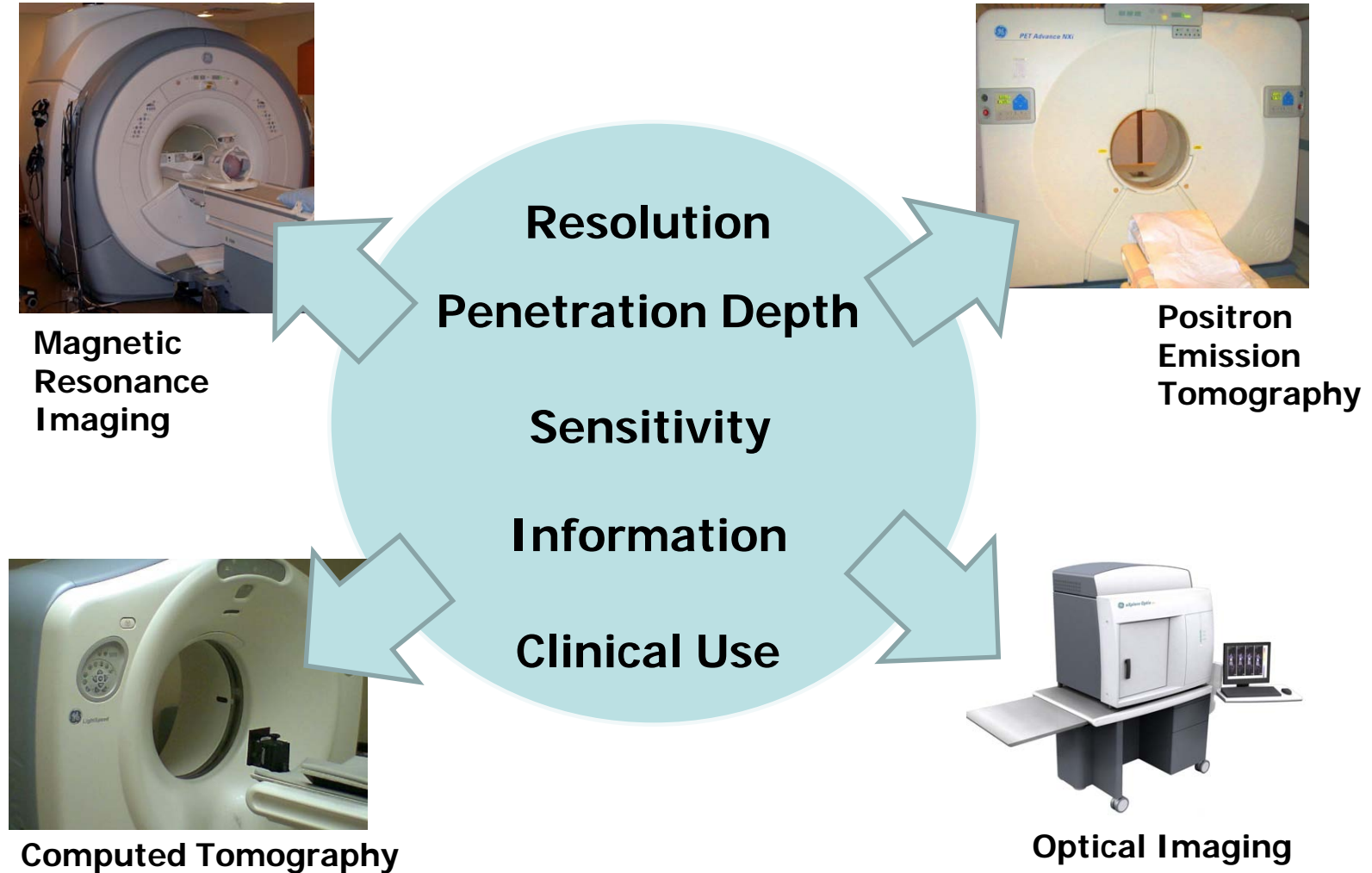
Imaging Systems

					
Imaging Technique	Spatial Resolution	Sensitivity ^b	Source of Imaging	Target	Tissue Penetrating Depth
MRI	> 7T, 25-300 μm Human 3T, 1mm	mM to μM (low)	Radiowave	Anatomical, physiological, molecular	No limit
CT	50-200 μm	not well characterized	X-ray	Anatomical, physiological	No limit
PET	1-2 mm	pM (high)	γ -ray	Physiological, molecular	No limit
Optical fluorescence Imaging	In vivo, 2-3 mm In vitro, sub- μm	nM to pM (medium)	Visible or near-infrared light	Physiological, molecular	< 1cm

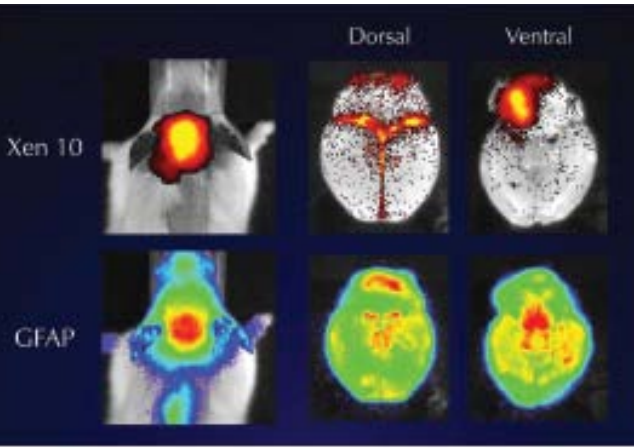
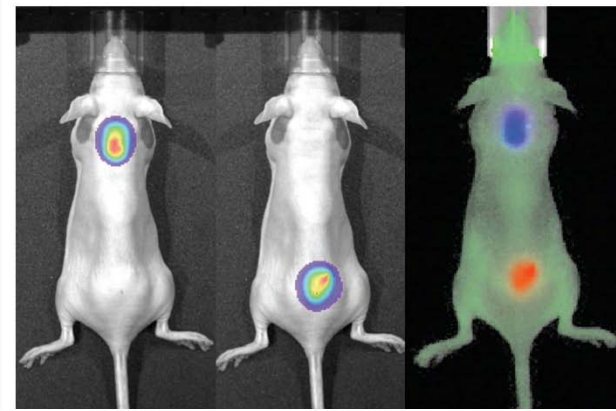
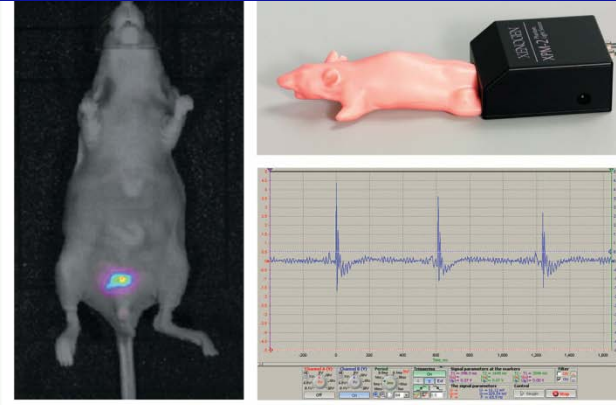
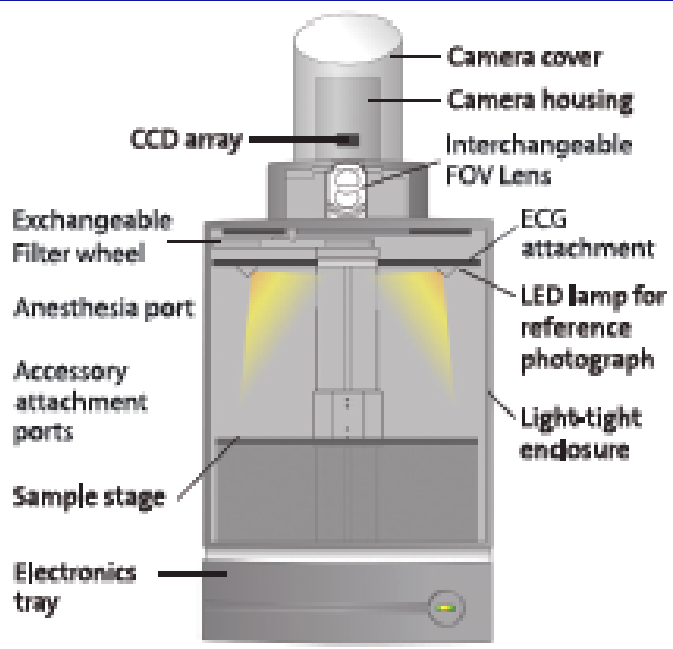
- For high-resolution, small-animal imaging systems (Clinical imaging systems are different)
- Sensitivity of detecting probe relative to background



Molecular Imaging Modalities

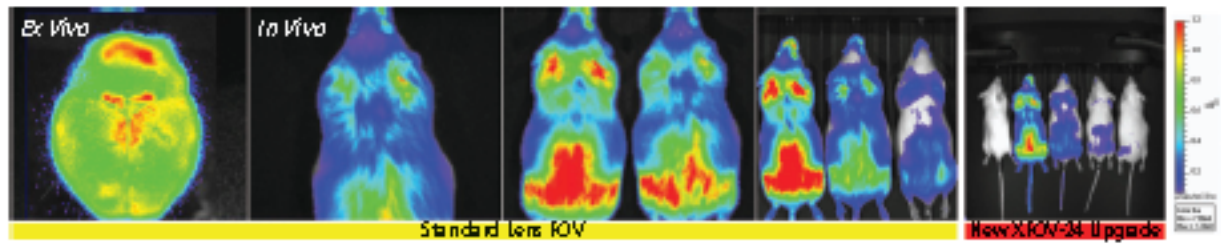


Near Infrared Fluorescence (NIRF) Imaging



Dual Reporter Imaging - High Resolution Ex Vivo Applications

Field of View

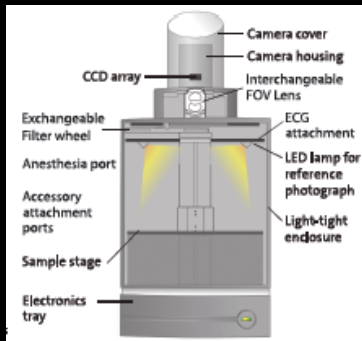


The MIS Lumina II Imaging System provides 5 fields of view.

Combination Technology with MR, NIRF, and Confocal Images



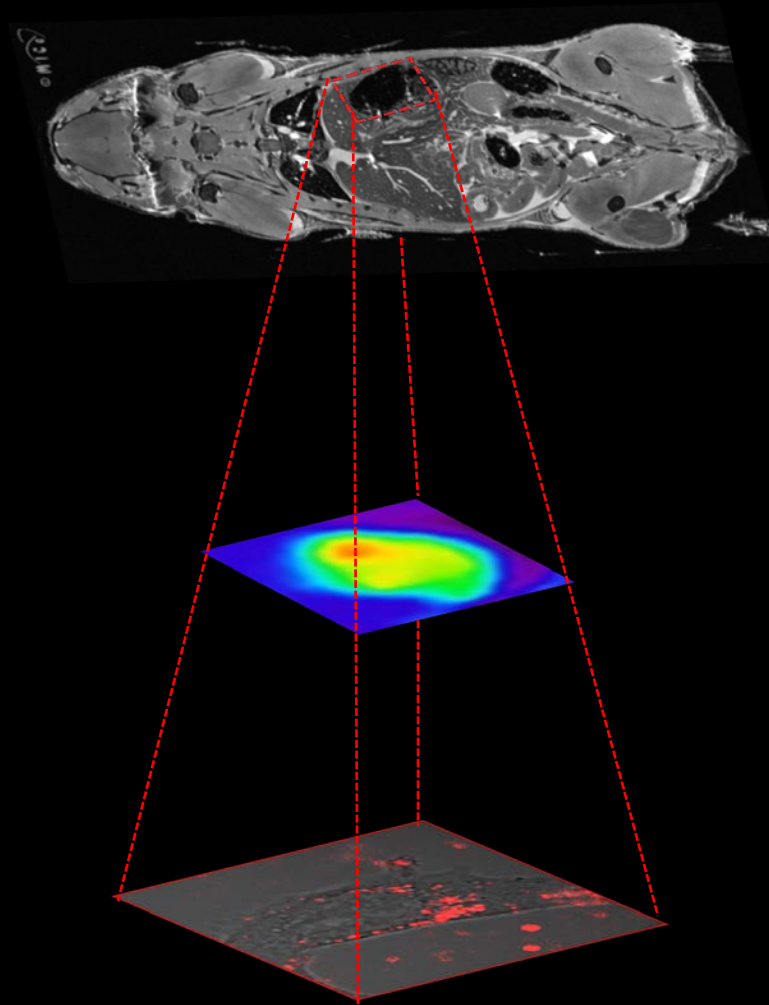
MR Imaging



NIRF Imaging



Confocal Imaging



A Whole Body Imaging



Specific tumors



Nanoparticles in
each tumor cell

Carbon nanotubes for drug delivery in-vivo

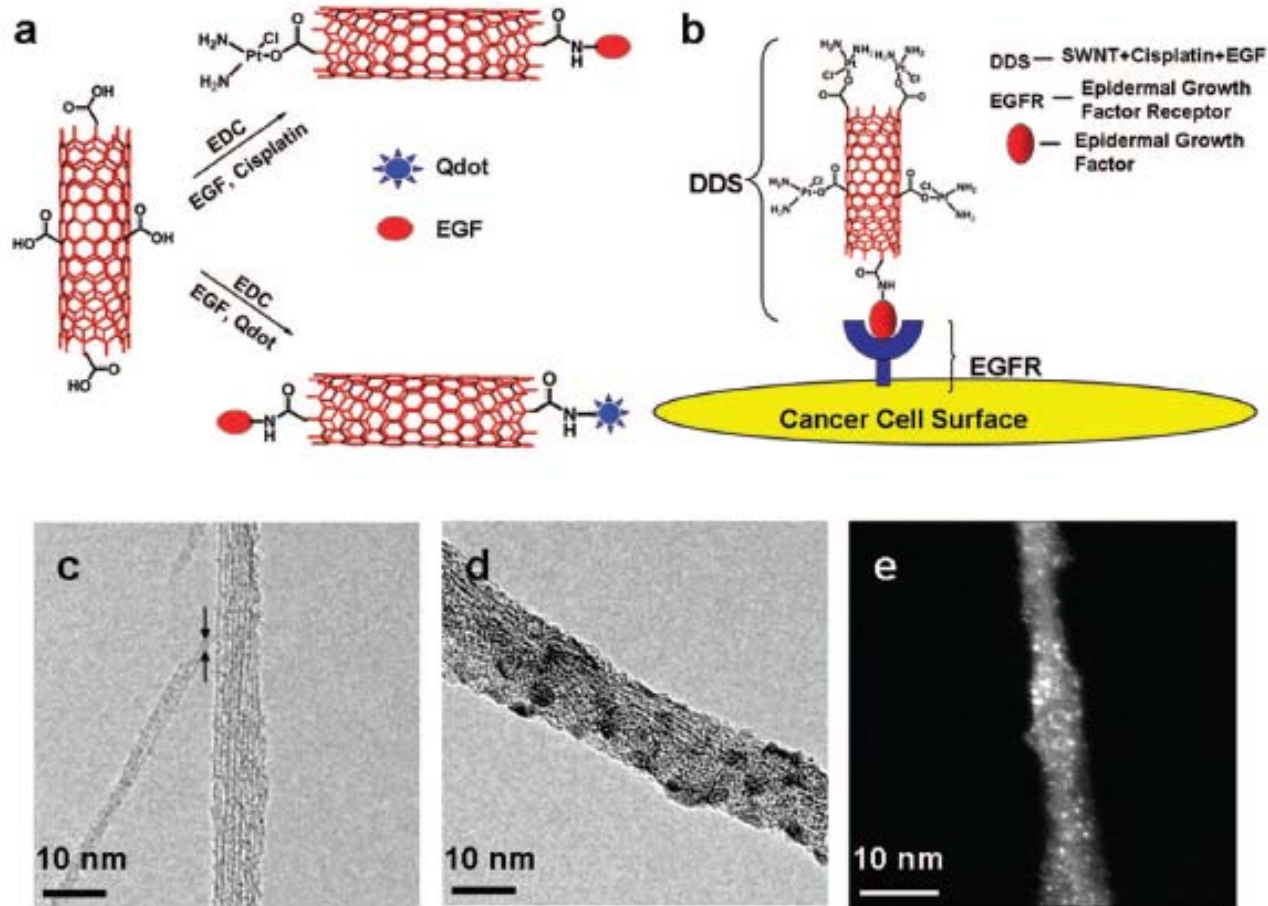


Figure 1. Nanotube-based delivery system. (A) Illustration of chemical reactions used to attach EGF, cisplatin, and Qdots onto carboxylated SWNTs (in red) using EDC as the coupling agent. (B) Schematic showing SWNT bundles bioconjugated with EGF and cisplatin targeting the cell surface receptor EGFR on a single HNSCC cell. Transmission electron micrographs of (c) oxidized SWNT bundles with arrows showing a single SWNT, (d) SWNT-Qdot-EGF bioconjugate bundle, (e) STEM image of SWNT bundle showing cisplatin as the bright spots. Source” **Birde et al. 2009**

Cellular internalization and selective uptake of carbon nanotubes

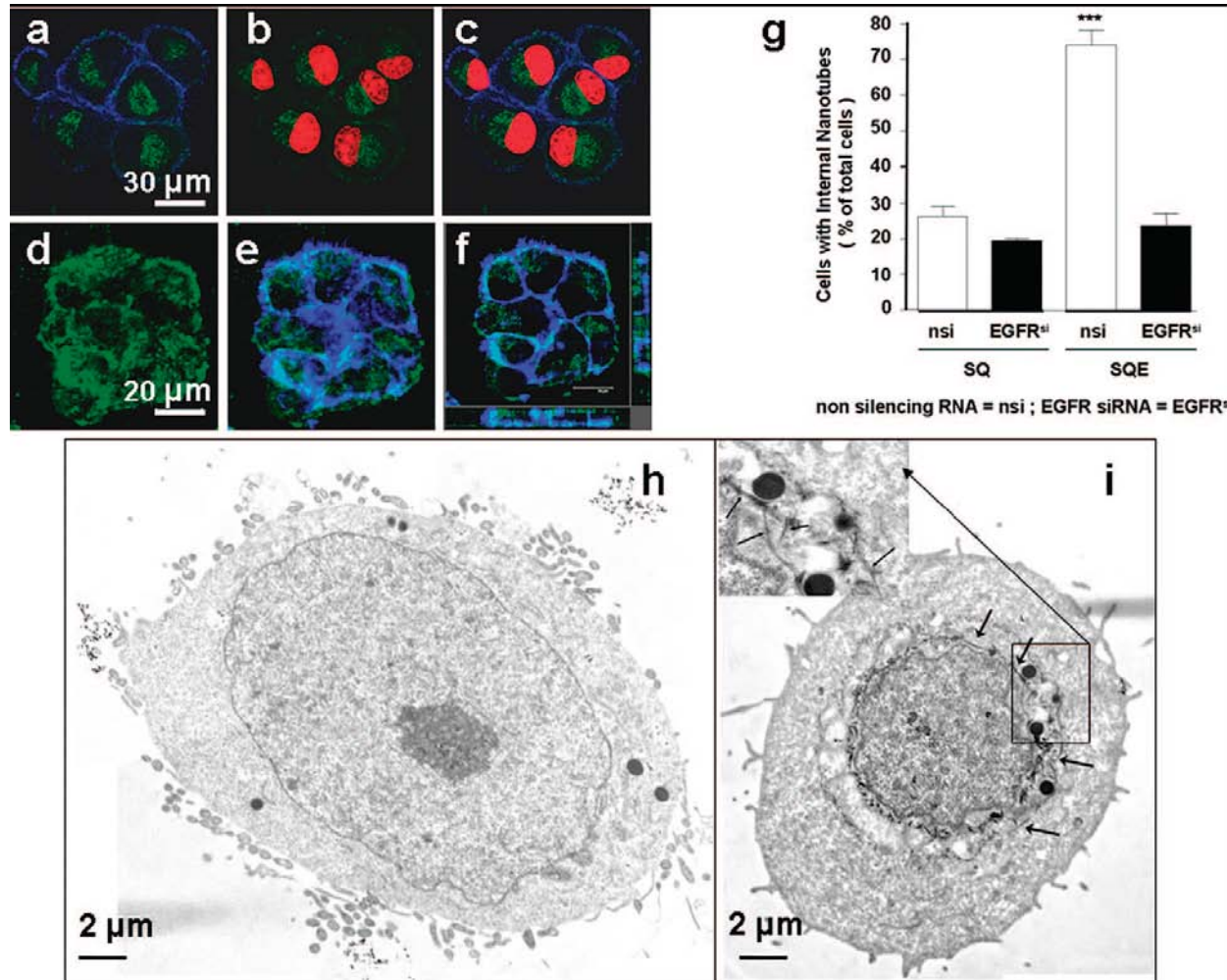


Figure 2. Cellular internalization and selective uptake of SWNT-Qdot525-EGF by HN13 cells. (a-c) z-Section micrographs of interiors of cells treated with SWNT-Qdot525-EGF (SQE) bioconjugates and analyzed by confocal microscopy: (a) images show the fluorescence of SQE (green) inside the cells and within the outer boundary limits of membrane as judged by actin stained by phalloidin (blue); (b) nuclei are illuminated with propidium iodide (red), and Qdots are seen in close proximity (green); (c) overlay of panels a and b showing internalization of SQE around the perinuclear region. (Scale bar = 30 μ m). 3D reconstitutions of confocal z-sections recapitulate the localization of Qdots (green) and within the periphery of actin fibers (blue) proximal to the cell membrane. (d, e) z-Stacked images showing (d) nanotube-Qdot color only; (e) with nanotube-Qdot and cell membrane colors; (f) three-dimensional reconstruction of panel e in xyz format. On the right is shown the z-stack going upward from the x axis; on the bottom is shown the z-stack going upward from the y axis. Scale bars = 20 μ m. (g) Quantification of results here and in Supporting Information, Figure S4 demonstrates that when the bioconjugate includes EGF and the cells retain high EGFR expression levels, the cells have the largest amount of bioconjugate internalization. The label EGFR^{si} means treatment with active siRNA to knockdown EGFR. t tests indicated significant differences between control/SQE and the other samples at $p < 0.05$ using ANOVA (***). (h, i) Cells incubated with SQ or SQE and subsequently washed and subjected to TEM: (h) cells exposed to SQ only, no features resembling internalized nanotubes detected; (i) cells treated with SQE show dark cylindrical structures resembling nanotubes (indicated by arrows) around the perinuclear region, presumably internalized bundles of SWNTs; the inset shows a higher magnification image with nanotubes indicated by arrows. Source: **Birde et al., 2009**

Detection of nanotube bioconjugates in tumors in vivo

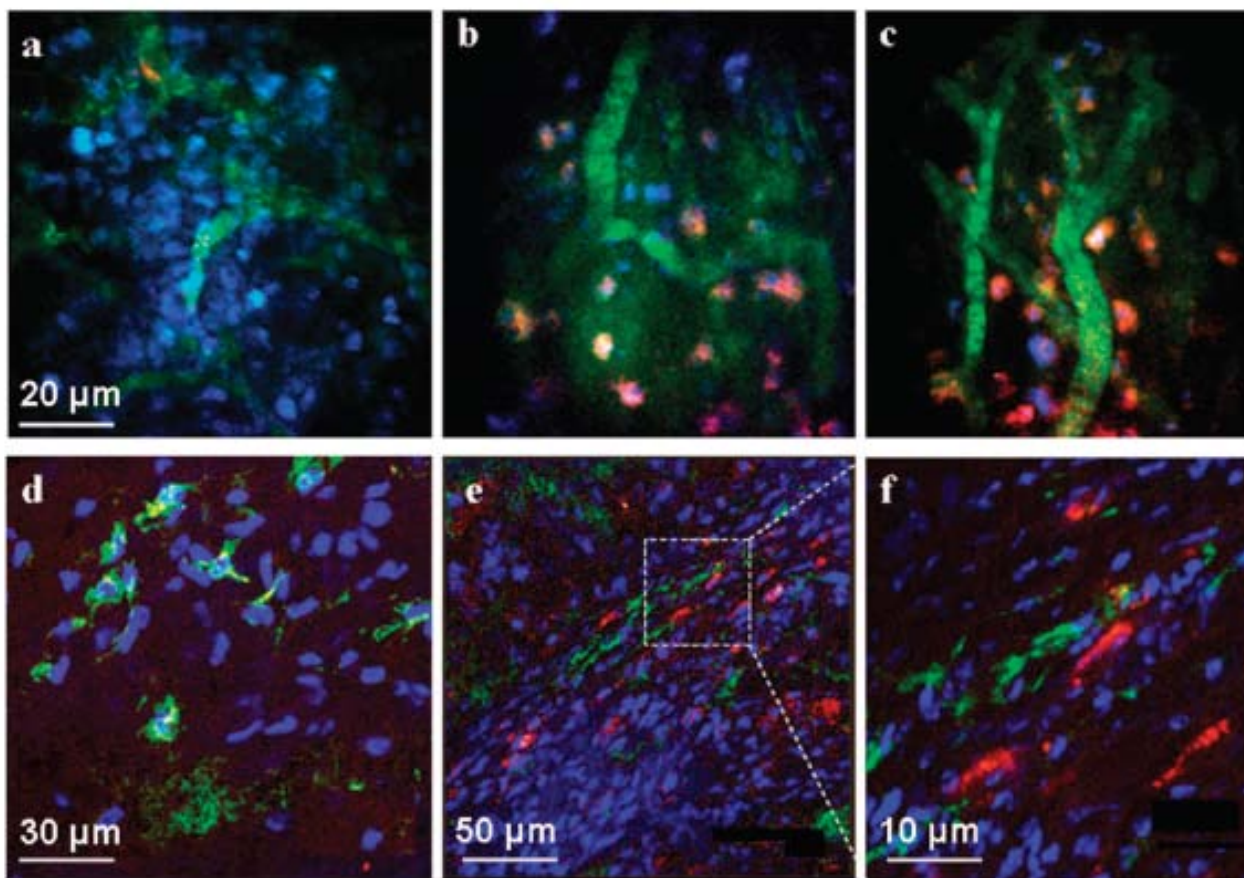


Figure 3. Detection of nanotube bioconjugates in tumors in vivo. Representative frames from time-lapse videos acquired by 3-color, intravital two-photon microscopy (a-c). Mice bearing the HN12 xenografts were anesthetized and treated with SQ or SQE (red) bioconjugates. Cell nuclei were stained with Hoechst (blue) and blood vessels with 500 kDa FITC-dextran (green): For SQ alone with no EGF (a), very little or no red fluorescence representing the Qdot signal was detected within the tumor mass 45 min after injection. Two different views after administration of SQE giving red fluorescence 45 min post injection within the tumor microenvironment (b,c). The red SQE bioconjugate is localized in close proximity to the nuclei suggesting its internalization by the tumor cells within the xenograft. (Scale bar in a-c is 20 μm). Confocal microscopy images of fixed xenograft cryosections (d-f). In the SQ treated tumor sections (d), only Hoechst stained cell nuclei (blue) and vascular FITC-labeled dextran (green) are visible (scale bar 30 μm). (e) In SQE treated mice, characteristic red fluorescence was widely distributed within the tumor microenvironment. (scale bar 50 μm). (f) Magnified dotted region of panel e showing internalized SEQ bioconjugates the cells within the tumor mass. Source: **Birde et al., 2009**.

Analysis of the distribution of nanotube bioconjugates in vivo

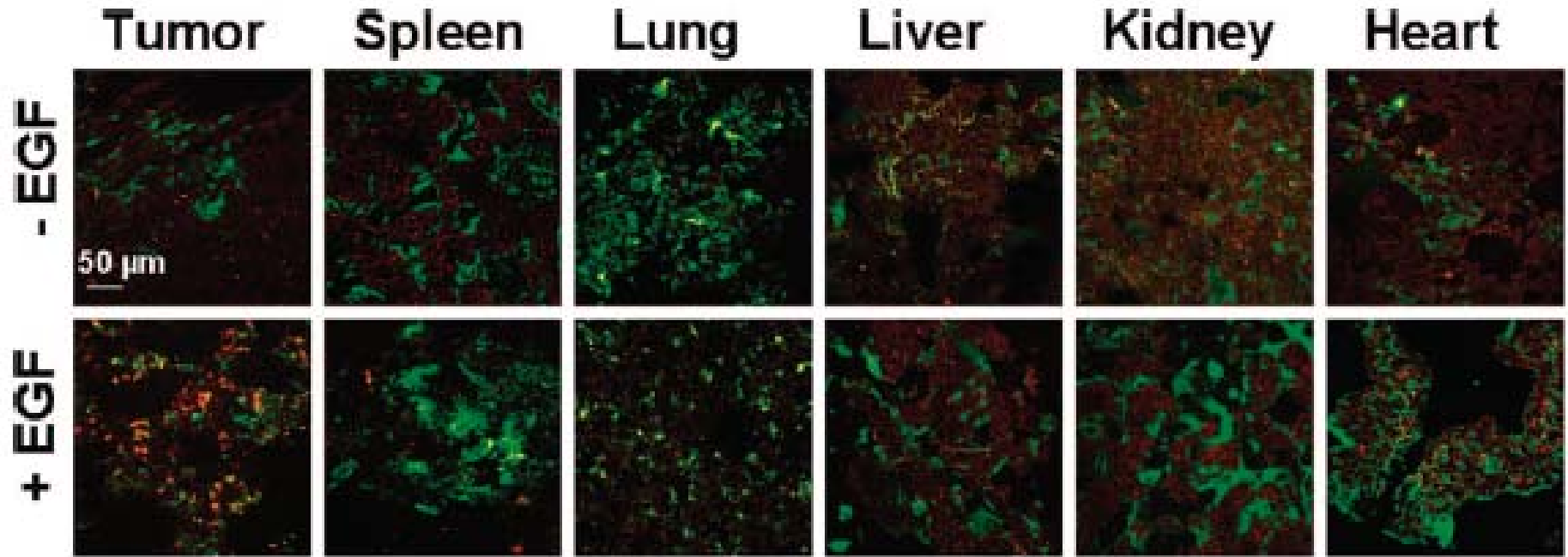


Figure 6. Analysis of the distribution of nanotube bioconjugates in vivo. Vital organs from tumor-bearing mice injected with Ho^{II} echst, FITC-dextran, then treated with either SQ or SQE, were removed, frozen, cryosectioned, fixed, and processed for confocal microscopy. Tumor tissues indicate increased uptake of bioconjugates, shown in red, only when EGF was on the nanotubes. Spleen, liver, kidney and heart show some red fluorescence characteristic of the SWNT□Qdots irrespective of the presence or absence of EGF. The pixel intensities were further analyzed for relative quantification of SQ or SQE levels within the different tissues (see supporting Figure S17). Source: **Birde et al. 2009**.

13.5 Evaluating therapeutic efficacy in-vivo

13.5.1 advantages of non-invasive measurements

13.5.2 measures of tumor load/shrinkage (tumor size, weight,...)

13.5.3 other measures of disease effects

13.5.3.1 direct measurement of restoration of lost or compromised functions

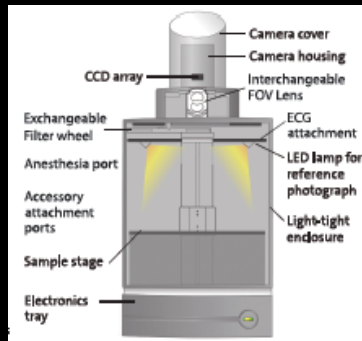
13.5.3.2 indirect measures of disease effects (e.g. behavior, weight gain/loss, .)

13.5.4 Some examples of in-vivo work with NMS

Combination Technology with MR, NIRF, and Confocal Images



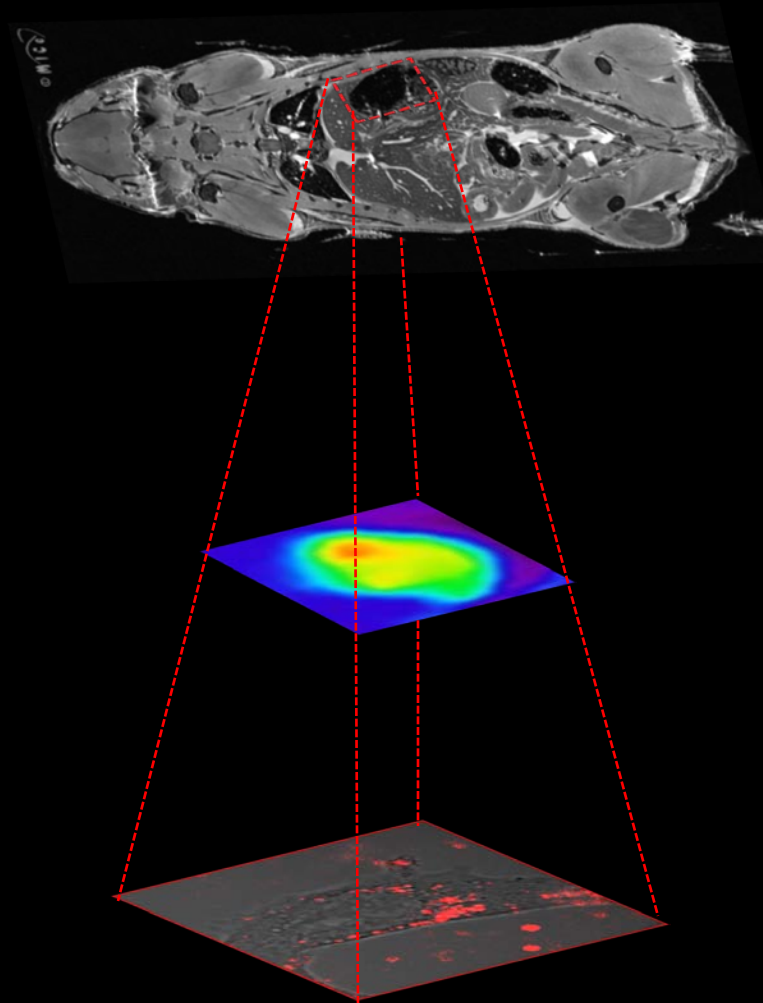
MR Imaging



NIRF Imaging



Confocal Imaging



A Whole Body Imaging

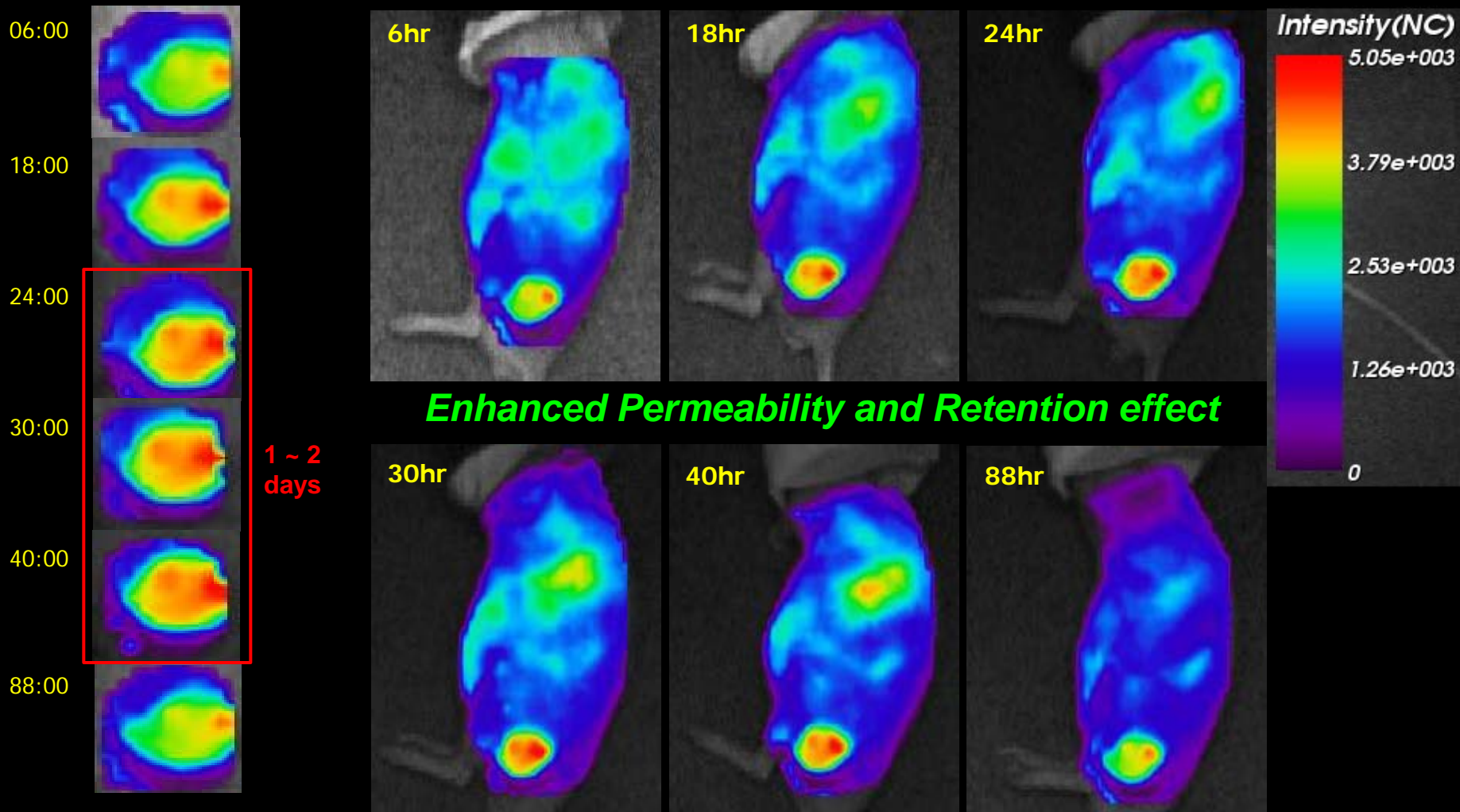


Specific tumors



Nanoparticles in
each tumor cell

In vivo results of HGC-Cy5.5-SPIOs



Selective killing of cancer cells using SWNT bioconjugates

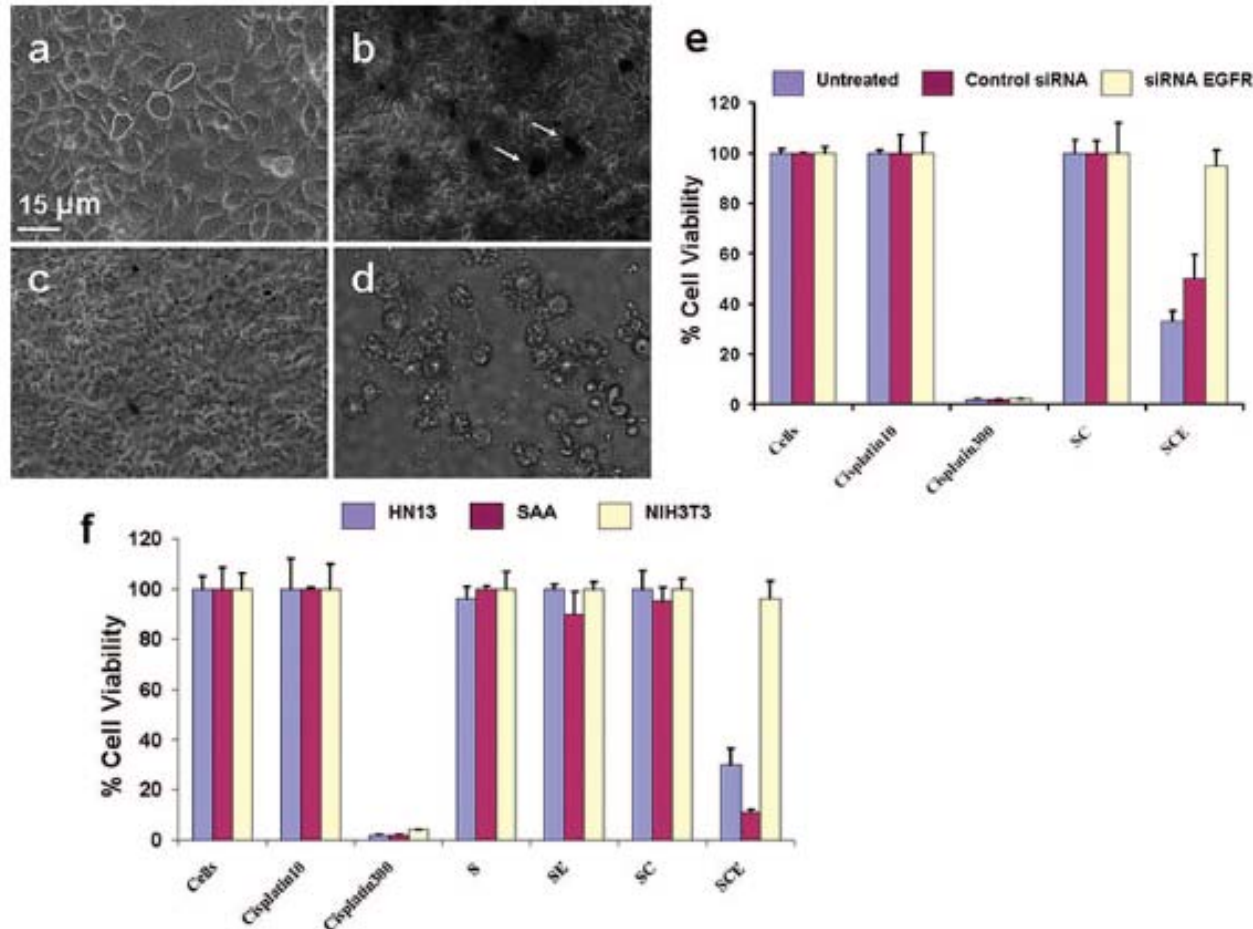


Figure 4. Selective killing of cancer cells using SWNT bioconjugates. (a-d) Optical micrographs showing targeting killing of HN13 cells with SWNT-cisplatin-EGF (SCE): (a) cells before treatment, which adhered to the plate and attached to each other with structural morphology intact; (b) cells treated with SCE for 10 min, before washing; dark regions are those with nanotubes present; (c) cells washed with PBS and resuspended in cell culture media DMEM after 10 min incubation with SCE; (d) HN13 cells (treated with SCE for 10 min and washed) after 12 h, cells appear floating detached from each other and the plate. Panels e and f are the cell viability studies. (e) Viability comparisons using cell proliferation assay after 12 h for normal HN13 cells, and HN13 cells transfected with EGFR knockdown and control (no knockdown, labeled "Untreated") siRNA: Cells, normal growth control; Cisplatin10, cells treated with 10 μ M free cisplatin; Cisplatin300, incubated with 300 μ M free cisplatin; SC, incubated with SWNT-cisplatin and washed with PBS after 10 min; SCE, incubated with SWNT-cisplatin-EGF (1.3 μ M cisplatin) then washed with PBS after 10 min. (f) Cell viability comparisons using cell proliferation assay after 12 h for normal HN13 cells, with NIH3T3 and SAA mouse fibroblast cells: Cells, normal growth untreated; Cisplatin10, cells treated with 10 μ M free cisplatin; Cisplatin300, incubated with 300 μ M free cisplatin; S, incubated with SWNTs 10 min; SE, incubated with SWNT-EGF and washed with PBS after 10 min. SC, incubated with SWNT-cisplatin and washed with PBS after 10 min; SCE, incubated with SWNT-cisplatin-EGF (1.3 μ M cisplatin) then washed with PBS after 10 min.

Source: Birde et al. 2009

Development of Docetaxel-encapsulated pegylated PLGA NP-Apt bioconjugates

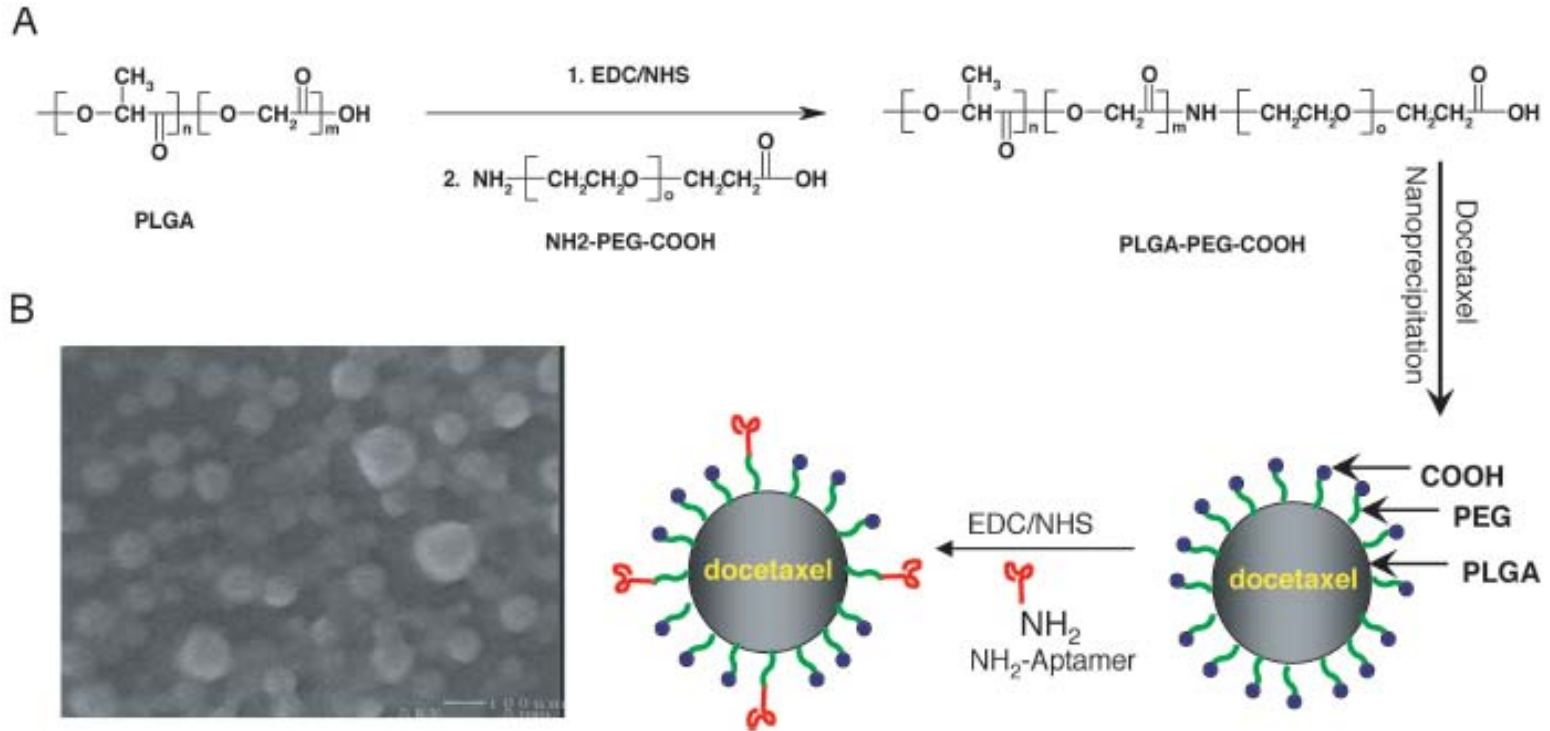


Fig. 1. Development of Dtxl-encapsulated pegylated PLGA NP-Apt bioconjugates. (A) Schematic representation of the synthesis of PLGA-PEG-COOH copolymer and strategy of encapsulation of Dtxl. We developed Dtxl-encapsulated, pegylated NPs by the nanoprecipitation method. These particles have a negative surface charge attributable to the carboxylic acid on the terminal end of the PEG. The NPs were conjugated to amine-functionalized A10 PSMA Apt by carbodiimide coupling chemistry. (B) Representative scanning electron microscopy image of resulting Dtxl-encapsulated NPs is shown. EDC, 1-ethyl-3-(3-dimethylaminopropyl)-carbodiimide; NHS, N-hydroxysuccinimide. Source: **Farokhzad et al., 2006**.

Comparative efficacy of treatments for human prostate cancer in nude mice

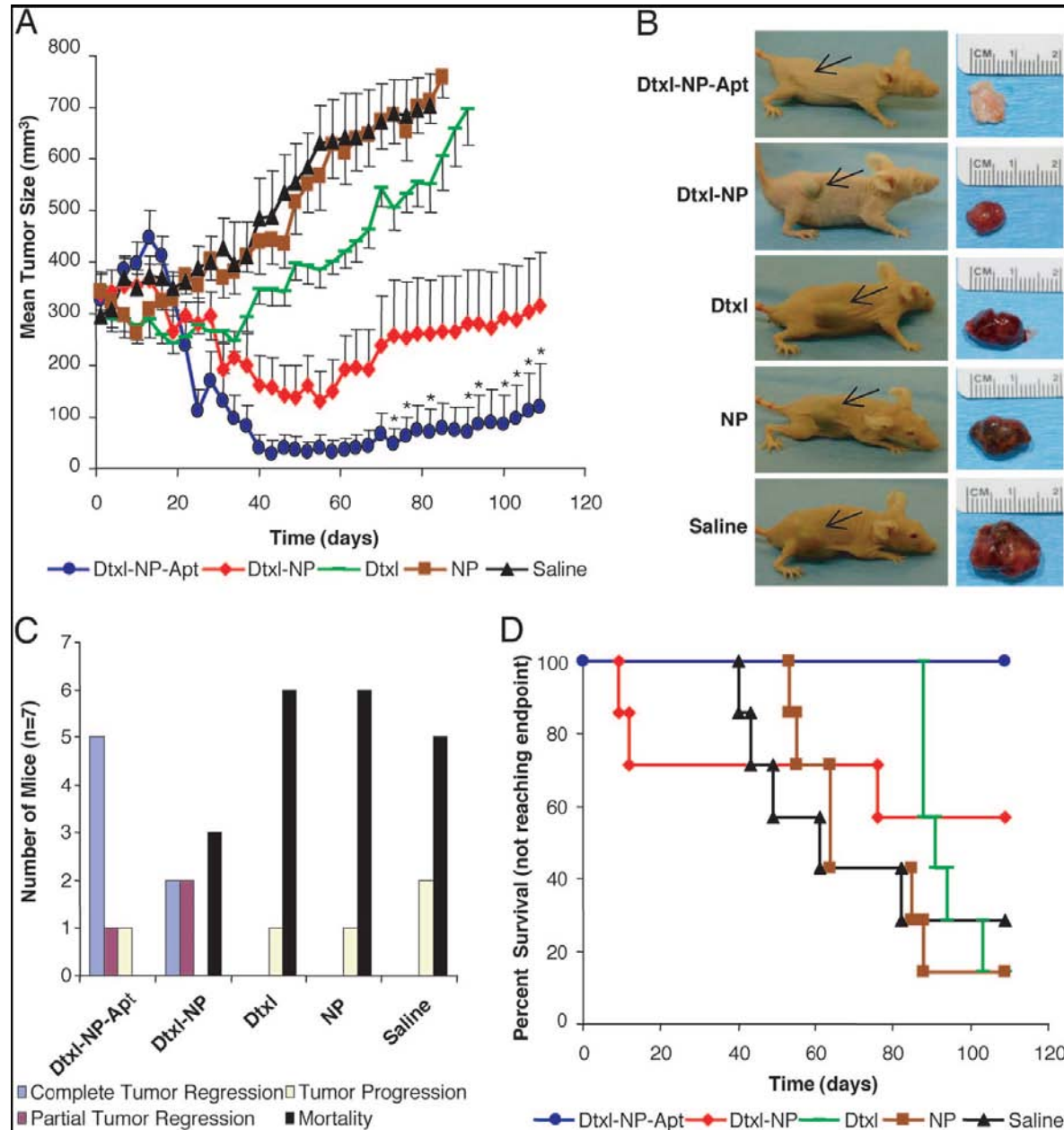


Fig. 3. Comparative efficacy study in LNCaP s.c. xenograft nude mouse model of PCa. (A) PCa was induced in mice by implanting LNCaP prostate epithelial cells s.c. in the flanks of nude mice and allowing the tumors to develop to appreciable size over 21 days (300 mm³). The comparative efficacy study of single intratumoral injection (day 0) of (i) saline (black); (ii) pegylated PLGA NP without drug (NP, brown); (iii) emulsified Dtxl (Dtxl, green), 40 mg/kg; (iv) Dtxl-capsulated NPs (Dtxl-NP, red), 40 mg/kg; or (v) Dtxl-encapsulated NP-Apt bioconjugates (Dtxl-NP-Apt, blue), 40 mg/kg was evaluated over 109 days and demonstrated that targeted NPs are significantly more efficacious in tumor reduction as compared with other groups. Data represent mean \pm SEM of seven mice per group. *, Data points for the Dtxl-NP-Apt group that were statistically significant compared with all other groups by ANOVA at 95% confidence interval. (B) Representative mouse at end point for each group is shown (Left) alongside images of excised tumors (Right). For the Dtxl-NP-Apt group, which achieved complete tumor regression, the scar tissue and underlying skin at the site of injection are shown. Black arrows point to the position of the implanted tumor on each mouse. (C) Plot of outcomes for each of the treatment groups divided into four categories: complete tumor regression (blue), incomplete tumor regression (red), tumor growth (yellow), and mortality (black). Two Dtxl-NP animals experienced 20% weight loss on days 9 and 12 after dosing and were euthanized. One mouse in each of the Dtxl and saline groups was euthanized late in the study for excessive weight loss likely attributable to large tumor load. (D) The Kaplan-Meier survival curve demonstrates that 100% of the Dtxl-NP-Apt group was alive on day 109, whereas the other groups had animals reaching our study end points and were euthanized on various days throughout the study period (end points defined as tumor load of 800 mm³ or BWL 20%).

Source: Farokzhad et al. 2006

Hyperthermic destruction of peri-tumor insertion of biomagnetic hydroxyapatite nanoparticles

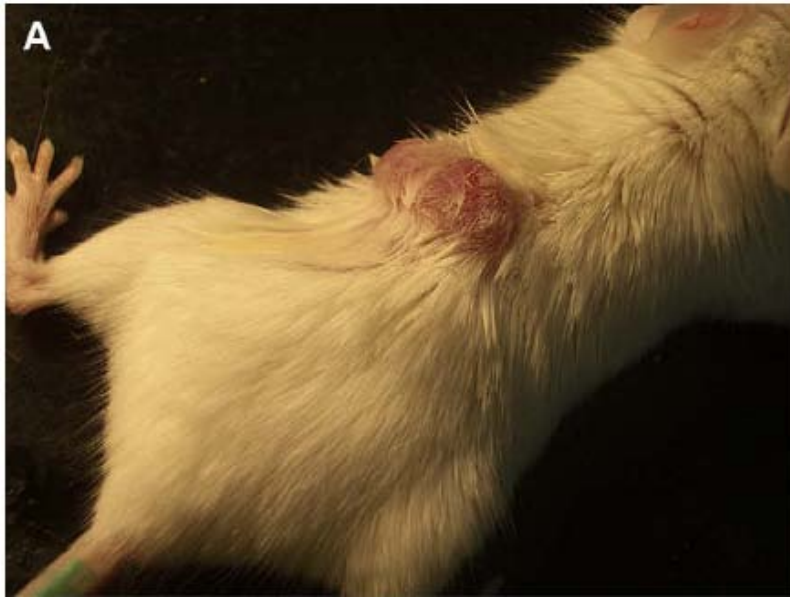


Fig. 3. The clinical photographs of the tumor in Group 6 (mHAP with magnetic field).

The tumor in day 1 (A), day 5 (B), and day 14 (C).

Source: **Hou et al. 2009**

13.6 Summary

- 13.6.1 Choosing an appropriate animal model and getting it approved takes time!
- 13.6.2 Animal experiments are expensive and time-consuming
- 13.6.3 Performing in-vivo measurements of drug delivery and therapeutic efficacy are more challenging and expensive than in-vitro or ex-vivo work!
- 13.6.4 But ultimately you must show that the NMS works in-vivo

References

Birde, A.A., Patel, V., Gavard, J., Zhang, G., Sousa, A.A., Masedunskas, A., Leapman, R.D., Weigert, R., Gutkind, J.S., Rusling, J.F. Targeted Killing of Cancer Cells in Vivo and in Vitro with EGF-Directed Carbon Nanotube-Based Drug Delivery. *ACS Nano* 3(2) 307-316 (2009).

Cartier, R., Kaufner, L., Paulke, B.R., Wustneck, R., Pietschmann, S., Michel, R., Bruhn, H., Pison, U. Latex nanoparticles for multimodal imaging and detection in vivo. *Nanotechnology* 18:195102 – 195113 (2007).

Cheng, J., Teply, B.A., Sherifia, I., Sunga, J., Luthera, G., Gua, F.X., Levy-Nissenbauma, E., Radovic-Morenob, A.F., Langer, R., Farokhzad, O.C. Formulation of functionalized PLGA–PEG nanoparticles for in vivo targeted drug delivery. *Biomaterials* 28: 869–876 (2007).

Farokhzad, O.C., Cheng, J., Teply, B.A., Sherifi, I., Jon, S., Kantoff, P.W., Richie, J.P., Langer, R. Targeted nanoparticle-aptamer bioconjugates for cancer chemotherapy in vivo. *PNAS* 103(6): 6313–6320 (2006).

Hou, C-H, Hou, S-M, Hsueh, Y-S, Lin, J., Wu, H-C, Lin, F-H The in vivo performance of biomagnetic hydroxyapatite nanoparticles in cancer hyperthermia therapy *Biomaterials* 30: 3956–3960 (2009).